

TOROIDAL RECIRCULATION, SADDLE-POINT TOPOLOGY, AND WALL-JET OUTWASH IN A TWIN-ROTOR SYSTEM IN GROUND EFFECT

Nishanth Pradyumna[1], Dr. Mogeng Li[2] & Prof. Dries Verstraete[3]

[1]PhD candidate, School of Aerospace, Mechanical and Mechatronic Engineering, The University of Sydney, Australia
[2]Lecturer, School of Aerospace, Mechanical and Mechatronic Engineering, The University of Sydney, Australia
[3]Professor, School of Aerospace, Mechanical and Mechatronic Engineering, The University of Sydney, Australia

Abstract

The outwash hazard and induced power penalty of multi-rotor ground-effect systems remain unresolved for rotor geometries of current multirotors. We report volumetric Shake-The-Box PIV of a twin-rotor system at a rotor centre-to-centre spacing of 3.5 radii and a ground clearance of 2 radii, with a three-blade HQProp propeller of 177.8 mm diameter. At ground level, downwash from each rotor turns radially outward into a wall jet that peaks at approximately 10 m/s, while the two jets collide and stagnate at the inter-rotor midplane. Q-criterion isosurfaces reveal a toroidal vortex beneath each rotor that spans from the disk plane to the ground. The inter-rotor centreplane vorticity field demonstrates four alternating concentrations with peak magnitudes of $\pm 1000\ s^{-1}$. It also captures a saddle point where fountain flow transitions to lateral toroidal outflow. The inward flow at a height of 1.0 radii above the ground reaches approximately 7 m/s, and the toroidal return limb reaches 10 to 15 m/s on the outer flanks of each rotor. Re-ingested flow enters the rotor disk at a lower stagnation pressure than ambient air and increases the induced power required to maintain thrust in hover.

Keywords: Volumetric PIV, Shake-The-Box, Multi-rotor, Ground effect, Wall jet, Toroidal recirculation, Outwash, eVTOL

1. Introduction

High-velocity outwash from rotors operating in ground effect poses a documented hazard to ground personnel and infrastructure at urban vertiports [1]. For conventional single-rotor helicopters, this wall jet is well characterised and exclusion zones are established on that basis. eVTOL aircraft introduce two complicating factors. Their disc loading is typically higher than that of helicopters of comparable gross weight [1, 2], which intensifies the induced velocity and strengthens the wall jet near the ground. Their distributed propulsion architectures also produce multiple interacting wakes that do not decay uniformly with radial distance [2]. The outwash topology of multi-rotor systems in ground effect is consequently governed by rotor-rotor interactions that have no equivalent in the single-rotor literature, and that remain insufficiently characterised [1].

For a single rotor operating in ground effect, the induced wall jet and the toroidal recirculation below the disk are well characterised. Tanner et al. [3] used phase-locked PIV and multi-hole probe rakes to show that the wall jet accelerates radially along the ground plane and peaks at a finite distance from the rotor axis. Bauknecht et al. [4] resolved the tip vortex geometry and trailing wake sheets at full scale and demonstrated the role of vortex impingement in sustaining the recirculation. These measurements define a reference state in which a single toroidal vortex sits below the disk, the wall jet spreads symmetrically along the ground plane, and the outwash field reflects the wake of one rotor alone. When a second rotor is added, the two wall jets interact at the inter-rotor midplane. This

produces a coupled flow topology that depends on rotor spacing and ground clearance and has no equivalent in the single-rotor case.

The aerodynamic interactions between side-by-side rotors alter the flow topology in ways that single-rotor measurements do not anticipate. Dekker et al. [5] applied volumetric Shake-The-Box particle tracking to characterise the flow across a parametric range of spacings and ground clearances and identified three flow regimes. Wakes merge at close spacing, a fountain forms at intermediate spacing, and the fountain is re-ingested into the rotor disks at wider spacing. Saddle points and toroidal recirculation structures were identified within the fountain-flow regime, and their unsteady switching behaviour was characterised in a follow-on study [6]. Lee et al. [7] extended this picture with a quasi-three-dimensional reconstruction from stacked planar PIV measurements and identified the saddle-point location and its dependence on spacing and ground clearance. The out-of-plane velocity component was not captured. Across these studies, neither the outwash velocity field nor the three-dimensional vortex topology has been resolved for representative rotor geometries.

The outwash velocity field near the ground governs the exclusion zones and personnel hazards identified in the preceding paragraph, yet it has not been measured in any multi-rotor ground-effect study to date. Dekker et al. [5] focused on the inter-rotor fountain region and Lee et al. [7] on the near-rotor flow structure. Neither resolved the radial wall jet at ground level across the full extent of the measurement domain. The three-dimensional topology of the coupled toroidal vortices has also not been visualised volumetrically for a rotor geometry representative of current multirotor hardware. This paper reports volumetric measurements of a twin-rotor system at $S/r = 3.5$ and $H/r = 2$ with a three-blade propeller representative of FPV and multirotor aircraft, and resolves both the outwash field and the three-dimensional vortex topology for this configuration.

We organised the remainder of the paper around three phenomena. Before we address those, Section 2. describes the twin-rotor hover rig and the volumetric particle tracking approach. Section 3.1 presents wall jet formation and ground stagnation. Section 3.2 resolves the toroidal recirculation structure as a three-dimensional vortex object. Section 3.3 characterises the three-dimensional saddle-point topology of the inter-rotor region, while Section 3.4 presents the outwash evolution with height.

2. Volumetric PIV of a twin-rotor hover rig

The coupled wall jet, toroidal recirculation, and saddle-point topology of multi-rotor flow in ground effect require simultaneous measurement of all three velocity components across the full inter-rotor volume. Volumetric Shake-The-Box particle tracking meets this requirement. It produces three-dimensional Lagrangian tracks without the out-of-plane ambiguity of planar PIV or the stacking assumptions of quasi-three-dimensional reconstruction.

2.1 Rotor setup

Each rotor used a three-blade HQProp J75 propeller (7×5×3, diameter 177.8 mm, geometric pitch 127 mm) driven by a BadAss 2310-900kv brushless DC motor. The rotors operated at 167 Hz (10,000 RPM) in still air to replicate hover at zero freestream velocity. At this operating point, the chord-based Reynolds number at $0.75r$ is approximately 59,900 and the tip Mach number is 0.27. The two rotors were phase-unlocked and the rotational speed was held to within $\pm$1% of the target value ($\pm$1.67 Hz). The HQProp J75 features the taper and camber distribution of propellers used in FPV drones and multirotor aircraft, in contrast to the rectangular untwisted NACA0012 blade used by Lee et al. [7]. The full set of geometric and operating parameters is given in Table 1.

The two rotors were arranged in a breaststroke counter-rotating configuration, with the blades on the inner side rotating toward each other. The rotor spacing S was defined as the centre-to-centre distance between the two rotor axes, and the ground clearance H as the distance from the rotor disk plane to the ground. For all measurements reported here, $S/r = 3.5$ and $H/r = 2$, as shown in Fig. 1. This configuration directs the downwash of both rotors into the inter-rotor gap, driving the wall jet collision that produces the fountain flow between them. The spacing can be adjusted up to $S/r = 4.0$ using a motorised linear actuator described in the following paragraph.

The motorised linear actuator positions the rotors with sub-millimetre resolution and full repeatability across runs. A Longs 17HS3410 stepper motor drives the carriage through a 26.8:1 gear reduction,

and an Arduino and Python interface commands the target separation. The gear reduction translates motor steps to sub-millimetre carriage displacement, and a microswitch at the minimum-spacing end stop re-establishes the same position on every run without manual realignment, as shown in Fig. 2. The actuator accommodates separations up to $S/r = 4.0$, which makes a parametric study of spacing effects possible in follow-on work. Repeatable positioning guarantees a well-defined flow state, and the volumetric measurement technique described in Section 2.2 was selected to resolve that state in three dimensions.

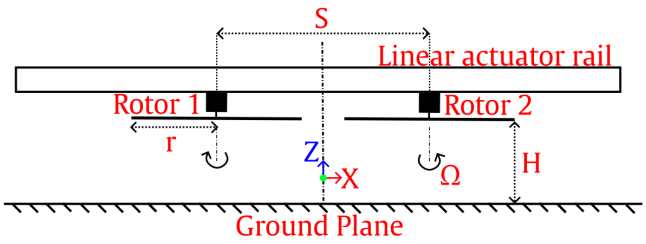


Figure 1 – Schematic of the twin-rotor hover rig. Two rotors are mounted on a linear actuator rail at centre-to-centre spacing S and ground clearance H. The rotor radius is r and the rotational speed is Ω. The coordinate origin is at the ground plane on the inter-rotor midplane, with z directed vertically upward. The rotors are arranged in a breaststroke counter-rotating configuration.

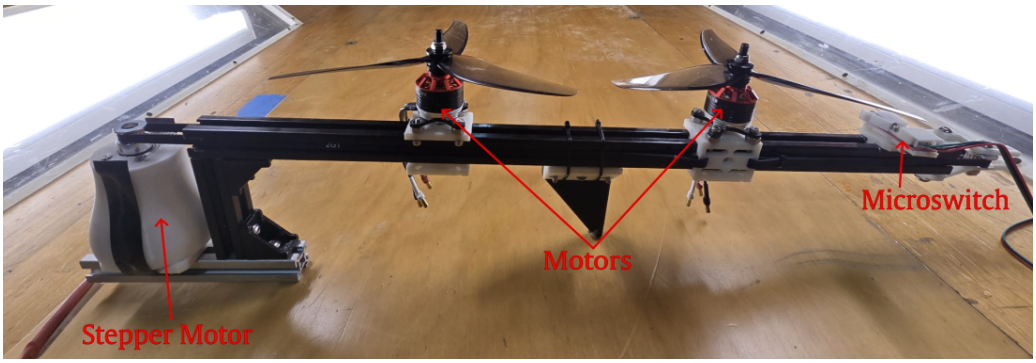


Figure 2 – The motorised linear actuator rig. The stepper motor drives the rotor carriage along the rail. The two brushless DC motors carry the rotor propellers. The microswitch at the right end stop re-establishes the home position on every run without manual realignment.

Table 1 – Two-rotor operating conditions

Rotor parameters and operation	
Rotation speed, Ω [Hz]	167 $\pm$1.67
Number of blades, B	3
Radius, r [mm]	88.9
Reynolds Number, Re_c	59,900
Tip Mach, M_{tip}	0.27
Lateral separation, S/r (centre-to-centre)	3.5
Rotor-to-ground standoff distance, H/r	2

2.2 Velocity Measurement

Four Phantom Miro 110 LAB cameras define a measurement volume of $0.6 \times 0.3 \times 0.3\,\mathrm{m}^3$ centred on the inter-rotor midplane, as shown in Fig. 3. The volume spans both rotor disks laterally and extends vertically from the disk plane to the ground. Two linear nozzle arrays of 1.5 m length, mounted upstream of the motors, introduce neutrally buoyant helium-filled soap bubbles of nominal diameter

0.3 mm into the inflow region before they are drawn through the rotor disk. A seeding density of 0.05 particles per pixel was achieved across the measurement volume.
A programmable timing unit synchronised the four cameras and the LED illumination panels. Images were captured at a frequency of 3500 Hz for 1s. Accurate three-dimensional particle localisation requires a geometric mapping between each camera's image plane and the measurement volume. We established this mapping with a geometric calibration with a pinhole camera model, followed by refinement using the volume self-calibration procedure of Wieneke [8], with a residual disparity of less than 0.1 pixels. A preprocessing pipeline enhanced image contrast, removed background noise, and masked the motor housings. We then passed the processed image sequences to the Shake-The-Box particle tracking algorithm [9], described in Section 2.3.

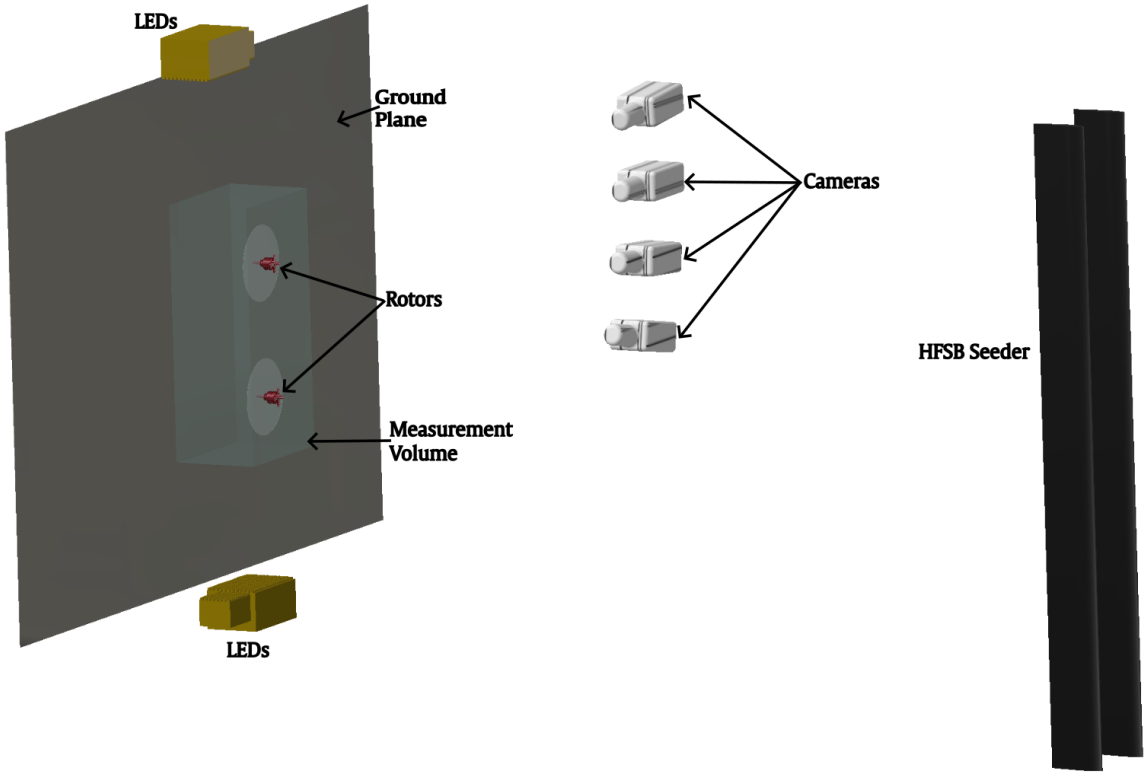


Figure 3 – Schematic of the volumetric PIV setup. Four cameras capture the measurement volume centred on the inter-rotor midplane. Two LED panels illuminate the volume from above and below. The HFSB seeder introduces neutrally buoyant helium-filled soap bubbles into the inflow region of the rotors.

2.3 Particle tracking

The Shake-The-Box algorithm [9] identifies individual particle positions across successive image frames and links them into three-dimensional Lagrangian tracks. At 3500 Hz over 3500 snapshots, the algorithm delivered an average of 25,000 tracks per timestep across the $0.6 \times 0.6 \times 0.3\,\mathrm{m}^3$ measurement volume. The maximum tracked particle displacement was approximately 10 voxels, which corresponds to a velocity of 20 m/s and is consistent with the peak flow velocities in the rotor wake. This peak velocity was independently verified with a Vectoflow 14-hole probe. The reconstruction method described below converts the Lagrangian tracks to a dense Eulerian velocity field on a regular grid.
Lagrangian tracks sample the flow at scattered positions and must be interpolated onto a regular grid before the velocity field can be analysed. We reconstructed the dense velocity field at each timestep with VIC# [10], an optimised implementation of the Vortex-in-Cell Plus method [11]. We used a grid spacing h of 8.03 mm, which resulted in a dynamic spatial range of DSR ≈ 75 and a dynamic velocity range of DVR ≈ 84. These reconstructed instantaneous velocity fields are subsequently averaged in time. The uncertainty of the time-averaged velocity field was estimated as $\varepsilon_u = \sigma_u/\sqrt{N}$, where σ_u is the

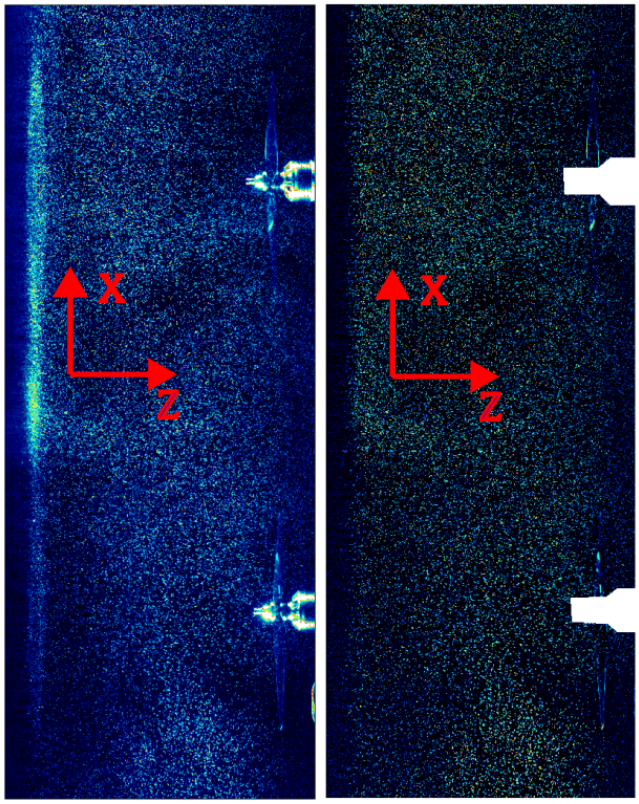


Figure 4 – Raw (left) and preprocessed (right) camera images of the measurement volume. The preprocessing pipeline enhances image contrast, removes background noise, and masks the motor housings (white regions, right).

local velocity standard deviation and $N = 3500$ snapshots. The domain-wide value is approximately 1.1% of the mean induced velocity $\bar{U} = 9.31$ m/s.

3. Results

Flow fields for multi-rotors that operate near the ground contain three coupled structures. A radial wall jet forms at ground level, a toroidal vortex sits beneath each rotor, and a saddle-point topology governs the inter-rotor midplane. The following subsections characterise them from observable signature to underlying cause. Together they resolve the outwash field and three-dimensional vortex topology identified in the introduction as absent from prior multi-rotor ground-effect studies.

3.1 Wall jet formation and ground stagnation

The horizontal radial velocity field at $z/r = 0.5$ reveals two dynamically distinct zones that characterise the near-ground flow (Fig. 5). Downwash from each rotor turns radially outward upon ground impingement, developing into high-velocity wall jets. On the outer flanks of the system, these outwash structures accelerate significantly; the left flank reaches a peak radial velocity of approximately 15 m/s, whereas the right flank exhibits a more intense acceleration, peaking between 20 and 23 m/s. At the inter-rotor midplane, the opposing streams collide, causing their radial momentum to arrest and bringing the local radial velocity down toward zero ($U_r \approx 0$ m/s). This stagnation zone subsequently forces the fluid upward to feed the inter-rotor fountain flow. Together, these high-velocity outwash zones and the central stagnation region define the ground-plane signature of the coupled vortex topology resolved in Sections 3.2 and 3.3.

A pronounced left-right asymmetry is visible across the time-averaged field. While both rotors generate strong outwash characteristics, the high-velocity region produced by the right rotor is far more expansive and intense, reaching the maximum scale limits of the outwash profile. This asymmetry in velocity magnitude and zone extent is highly consistent with the unsteady fountain-switching behaviour documented by Dekker et al. [6], who demonstrated that re-ingestion and wake bias alternate

aperiodically between side-by-side rotors. An imbalance in the cumulative time spent in one preferred switching configuration during the sample window manifests as this asymmetric radial velocity distribution within the time-averaged frame.

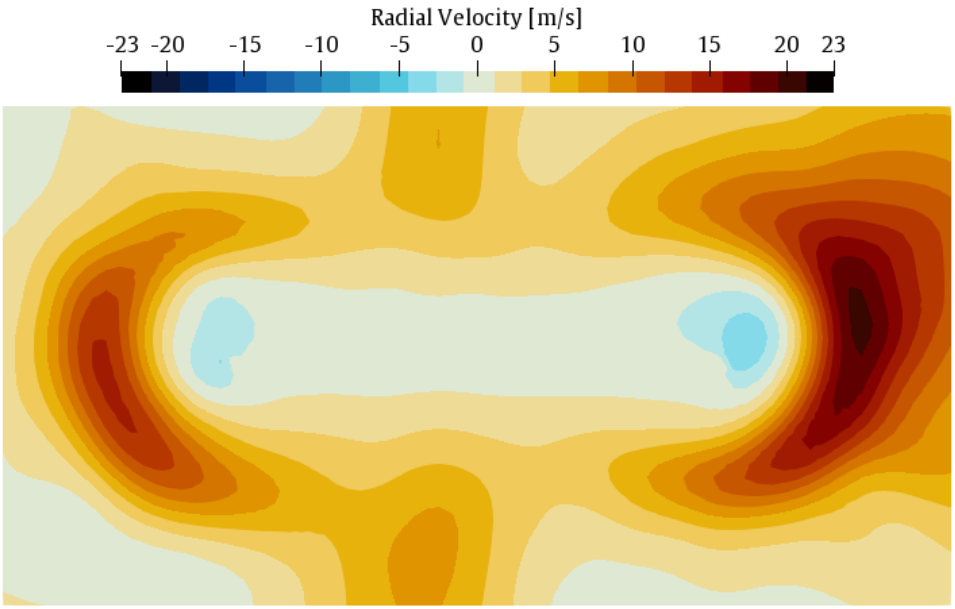


Figure 5 – Time-averaged radial velocity U_r in the horizontal plane at $z/r = 0.5$ ($z = 44.45$ mm). The absolute velocity scale spans from -23 m/s to 23 m/s. Outwash wall jet structures are prominent on both flanks, with the right rotor flank exhibiting a significantly higher peak radial velocity reaching approximately 20 to 23 m/s, compared to a peak of roughly 15 m/s on the outer left flank.

3.2 Toroidal recirculation structure

The wall jet at ground level marks where rotor downwash has turned and propagates radially outward, but it does not reveal the three-dimensional vortex structure that drives that turning. Q-criterion isosurfaces identify such coherent rotating regions by the condition that the rotation rate dominates the strain rate. They expose the recirculation beneath each rotor as a volumetric toroid rather than a planar cross-section (Fig. 6).

Each rotor produces a distinct toroidal structure that spans from the rotor disk plane to the ground. The tip vortex is shed at the blade tips where velocities reach 15–17 m/s. The rotor downwash carries high momentum as it leaves the disk plane, and this momentum decays as the structure convects downward through the ground turn. A separate inner tube structure marks the hub vortex at the rotor centre. The high-velocity downwash between the two structures falls below the Q-criterion threshold and does not appear on the isosurface. At $S/r = 3.5$, the two toroids do not merge, consistent with the fountain-flow regime identified by Dekker et al. [5].

The two toroids are not identical in the time-averaged field. The left rotor exhibits a fragmented annular skirt at the base of its toroid, absent from the right. This asymmetry persists across the full one-second average despite the phase-unlocked rotor operation, which suggests a difference in mean flow state rather than a transient feature. The same left-right asymmetry is evident in the wall jet field at $z/r = 0.5$ (see Section 3.1), and both are consistent with an asymmetric mean re-ingestion state of the kind reported by Dekker et al. [6].

3.3 Three-dimensional saddle-point topology

The time-averaged vertical velocity field in the inter-rotor centreplane demonstrates a saddle-point topology that connects the fountain flow to the two toroidal recirculations (Fig. 7). The streamlines show where the upward momentum of the fountain is exhausted and the flow bifurcates laterally. At a critical height in the inter-rotor midplane, fountain streamlines converge from below while toroid streamlines diverge laterally. This bifurcation structure is the saddle point of the inter-rotor flow field, where the fountain meets two counter-rotating toroidal recirculations.

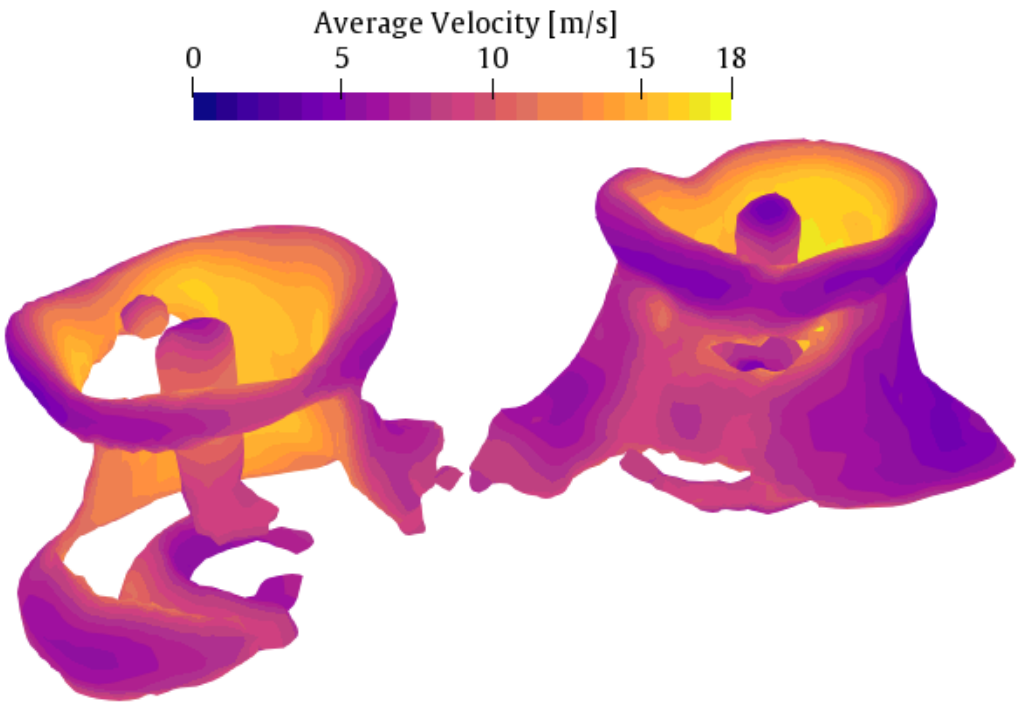


Figure 6 – Q-criterion isosurface at $Q = 10^5$ s^{-2}, coloured by velocity magnitude. Each rotor produces a toroidal structure that spans from the disk plane to the ground. Velocities reach 15–17 m/s at the blade tips and decay toward the base. An inner hub vortex tube is visible at the rotor centre. The left rotor exhibits a fragmented annular skirt at the base of the toroid, absent from the right rotor in the time average.

The vorticity field in the inter-rotor centreplane reveals the sign and strength of the two counter-rotating toroidal recirculations (Fig. 8). Each toroid contributes two vorticity concentrations to the centreplane, one from its inner limb and one from its outer limb. The four concentrations alternate in sign across the span, with peak magnitudes of approximately 1000 s^{-1}. The sign change matches the breaststroke configuration where each toroid rotates in the opposite sense to its neighbour. Each concentration has an elongated crescent cross-section as expected for a toroidal core whose axis curves away from the centreplane. The two toroids are separated and their inner vorticity arcs do not merge. This matches the fountain-flow regime expected at our rotor spacing of $S/r = 3.5$ [5].
The four-concentration centreplane topology and toroid separation are consistent with the fountain-flow regime of Dekker et al. [5] and resolve the saddle-point structure identified by Lee et al. [7] volumetrically. Dekker et al. identified saddle points from volumetric STB PIV across a parametric range of spacings but did not present a centreplane vorticity field, and their measured cases bracket the present configuration at $S/r = 3.5$. Lee et al. quantified the saddle-point location from stacked planar measurements but did not capture the out-of-plane velocity component and could not resolve the volumetric vortex topology. The present centreplane vorticity field further resolves the sign alternation and toroidal geometry of both recirculations at $S/r = 3.5$, which neither the centreplane velocity of Dekker et al. nor the quasi-3D reconstruction of Lee et al. could provide. The radial velocity field at ground level, absent from both prior studies, is characterised in Section 3.4.

3.4 Outwash evolution with height

At $z/r = 1.0$, the horizontal radial velocity field (Fig. 9) transitions away from the centralized stagnation pattern observed closer to the ground, displaying asymmetric outwash rings centered around each rotor axis. The right rotor generates a notably more intense flow signature, with peak outward velocities reaching approximately 10 m/s on its outer flank, compared to roughly 8 m/s on the left counterpart. Concurrently, the interaction structures generate narrow, high-velocity outwash channels propagating vertically along the inter-rotor midplane, carrying fluid outward at speeds up to 10 m/s.
The full-height structure of the outwash and its corresponding re-ingestion pathways are captured

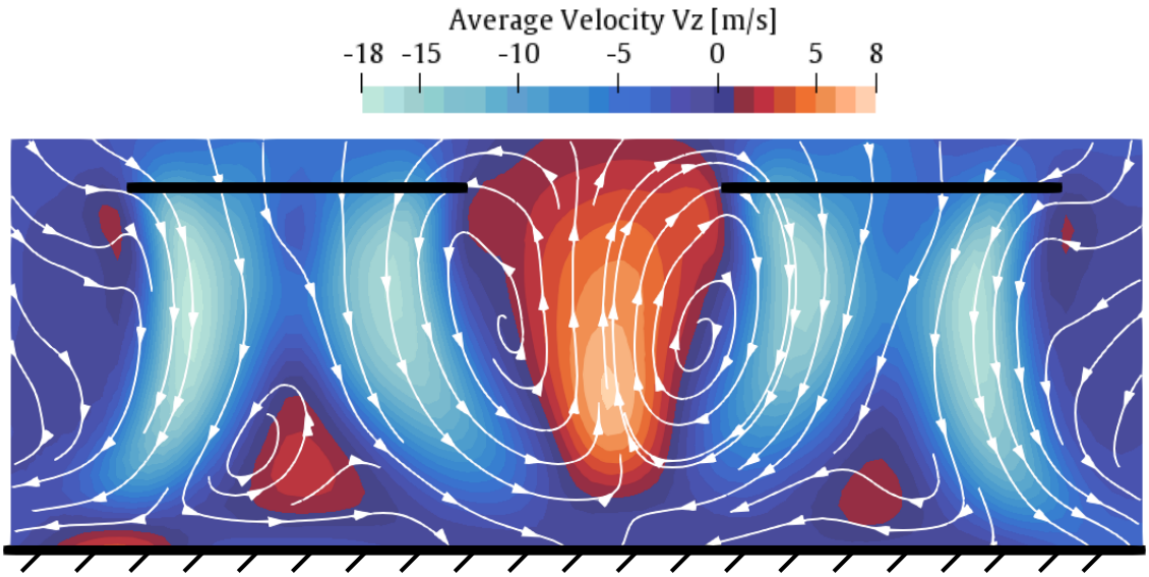


Figure 7 – Time-averaged vertical velocity and streamlines in the inter-rotor centreplane. At a critical height, fountain streamlines converge from below while toroid streamlines diverge laterally. This bifurcation defines the saddle point of the inter-rotor flow field.

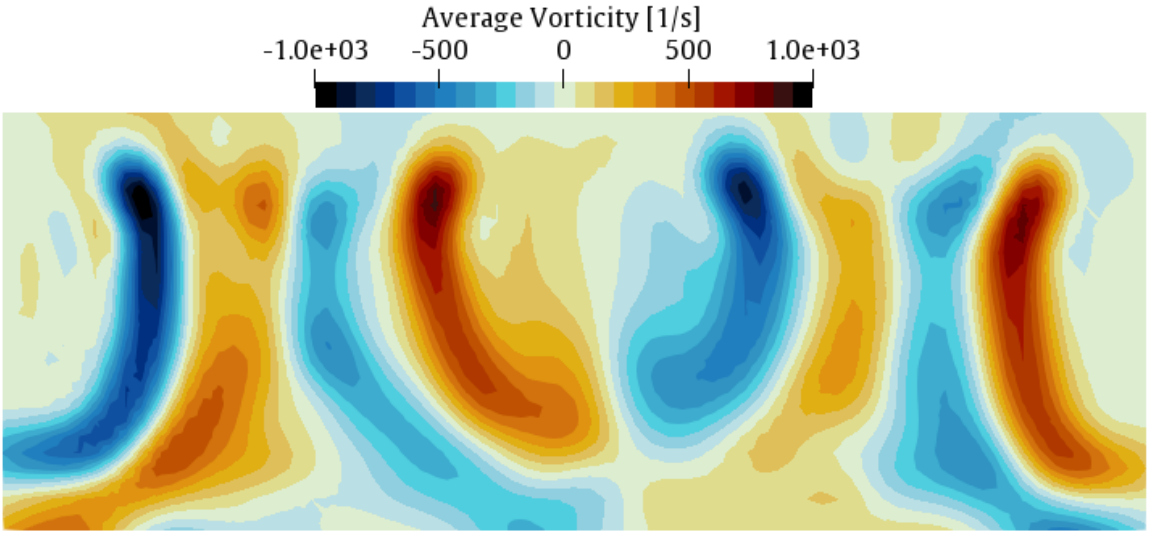


Figure 8 – Time-averaged spanwise vorticity in the inter-rotor centreplane. Four concentrations alternate in sign across the span, with peak magnitudes of approximately ± 1000 s^{-1}. Each toroid contributes two concentrations of opposite sign. The elongated crescent cross-sections reflect the curvature of the toroidal vortex axis. The inner vorticity arcs do not merge, consistent with toroid separation at S/r = 3.5.

clearly via the vertical cross-section cutting through the rotor axes (Fig. 10). At ground level along the bottom boundary, downwash impingement produces high-velocity wall jets that accelerate outward. This outwash layer exhibits a major left-right power asymmetry; the left jet peaks near 16 m/s, whereas the right jet undergoes extreme acceleration, exceeding 23 m/s as it shears along the surface.

In the inter-rotor zone between the axes, the opposing ground-level streams collide, completely arresting the radial momentum ($U_r \approx 0$ m/s) before deflecting the fluid upward into the fountain. As this upward fountain flow approaches the rotor disk plane, it splits and feeds into the upper recirculation zones. On the outer flanks near the upper boundaries, this structural loop is completed by high-velocity inward-directed return limbs. These ingestion zones manifest as concentrated negative velocity cores peaking around -10 m/s, drawing fluid back toward the rotor disks at a reduced

stagnation pressure and setting the primary aerodynamic constraint on multi-rotor hover efficiency.

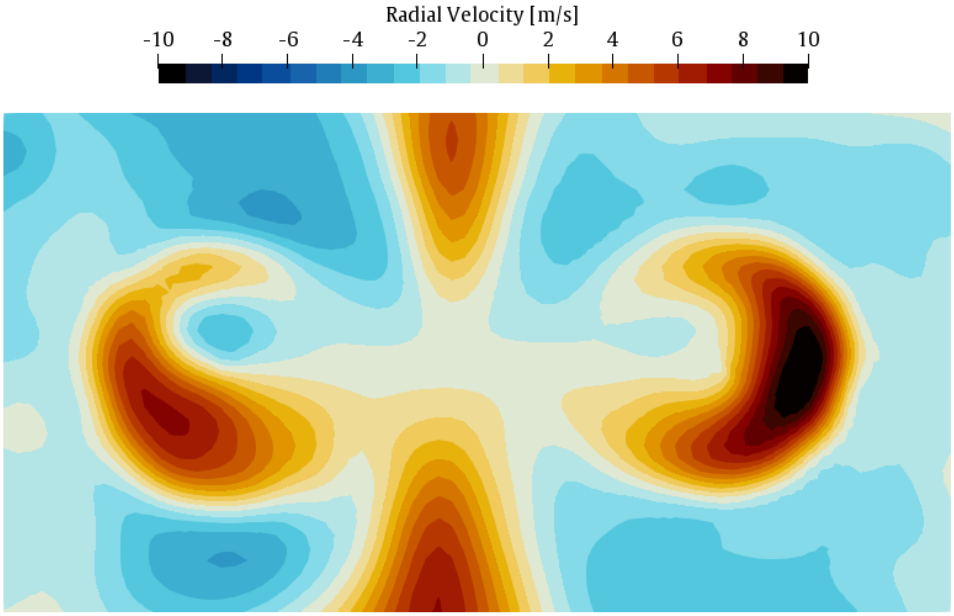


Figure 9 – Time-averaged radial velocity U_r in the horizontal plane at $z/r = 1.0$ ($z = 88.9$ mm) Each rotor produces a distinct asymmetric ring of positive (outward) velocity. The outwash features are significantly stronger on the right rotor's flank, where local peaks reach approximately 10 m/s, while the left rotor's flank peaks around 10 m/s. Pronounced cross-axis outwash lanes extend vertically along the inter-rotor midplane, displaying positive velocities up to 10 m/s.

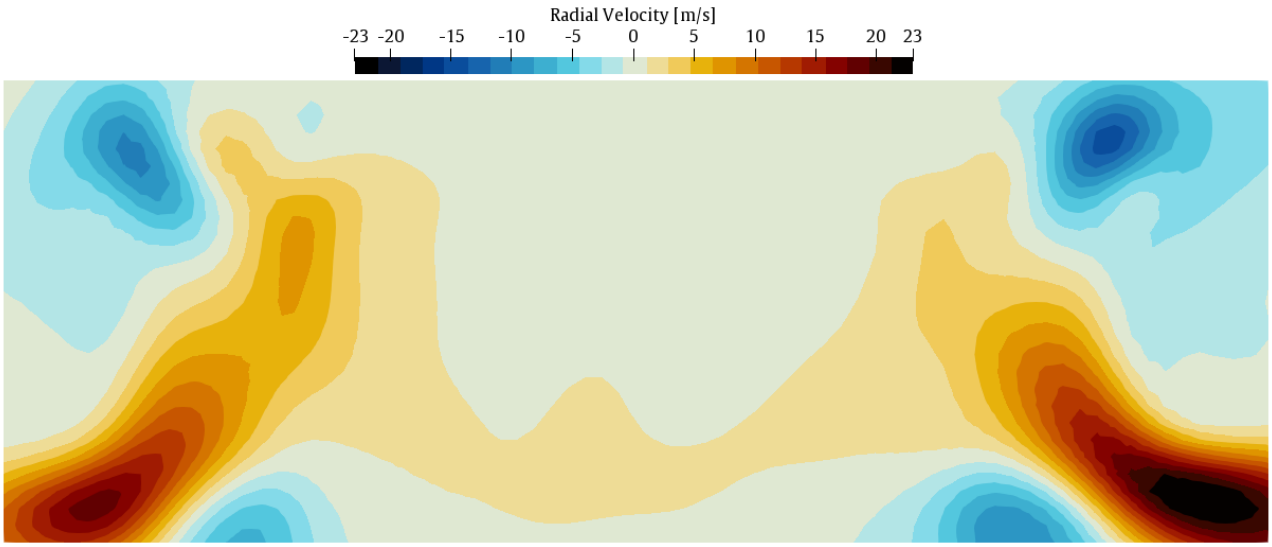


Figure 10 – Time-averaged radial velocity U_r in a vertical slice cutting through each rotor axis. The intensified outward wall jet is prominent at ground level, with a severe asymmetry showing the right outwash layer peaking at the maximum color scale limits (> 23 m/s). Well-defined negative (inward-directed) velocity cores appear near the upper boundary on the outer flanks, reaching values around -10 m/s, tracking the high-speed return limb of the toroidal recirculation.

The outwash and re-ingestion fields characterised above have two distinct operational consequences. The ground-level wall jet poses a direct hazard to ground personnel and infrastructure. Exclusion zone standards derived from single-rotor helicopter data do not account for the inter-rotor stagnation and fountain structures. They alter the spatial distribution of outwash relative to either rotor in isolation [1]. Re-ingested flow has passed through the ground turn and enters the rotor disk at a lower stagnation pressure than ambient air. This reduces the effective inflow quality at the rotor disk and

increases the induced power required to maintain thrust in hover. Together, the outwash hazard and the induced power penalty set aerodynamic constraints on rotor spacing and ground clearance that single-rotor ground-effect data cannot supply.

4. Conclusion

Our measurements address three gaps left by prior volumetric and quasi-three-dimensional studies of multi-rotor ground-effect flow. Prior studies neither measured the outwash velocity field at ground level nor resolved the three-dimensional toroid geometry beyond planar slices and regime schematics. Prior work also did not present the centreplane vorticity field. At $S/r = 3.5$, this vorticity field identifies the saddle-point topology and toroid limb structure. We captured four vorticity concentrations that alternate in sign at peak magnitudes of ± 1000 s^{-1} and identify the inner and outer limbs of both toroids. These coupled structures have two direct operational consequences.

The ground-level wall jet and the toroidal return limb impose aerodynamic constraints on ground clearance that single-rotor ground-effect data cannot quantify. Exclusion zone standards derived from single-rotor data do not account for the inter-rotor stagnation zone and fountain structure. These alter the spatial distribution of outwash relative to either rotor in isolation. Re-ingested flow accelerates into an asymmetric ground outwash layer exceeding 23 m/s on the dominant flank, returns as an inward-directed limb at 10 to 15 m/s, and enters the rotor disk at a lower stagnation pressure than ambient air. This stagnation pressure deficit increases the induced power required to maintain thrust in hover. Both penalties depend on rotor spacing and ground clearance in ways that a parametric study can now quantify.

The measurements reported here establish the coupled flow topology at $S/r = 3.5$ and $H/r = 2$ as a reference state for a parametric study of rotor spacing and ground clearance. The motorised linear actuator accommodates separations up to $S/r = 4.0$ with sub-millimetre repeatability. A parametric study across rotor spacing and ground clearance will map the outwash field and volumetric vortex topology at conditions that prior regime classifications did not characterise. It will also establish the regime boundaries at which the outwash hazard and re-ingestion penalty change character. These boundaries are the aerodynamic design inputs that rotor placement in eVTOL vehicles currently lacks.

5. Contact Author Email Address

For further communication, please contact the corresponding author's email:
Nishanth Pradyumna, mailto: Nishanth.Pradyumna@sydney.edu.au

6. Copyright Statement

The authors confirm that they, and/or their company or organization, hold copyright on all of the original material included in this paper. The authors also confirm that they have obtained permission, from the copyright holder of any third party material included in this paper, to publish it as part of their paper. The authors confirm that they give permission, or have obtained permission from the copyright holder of this paper, for the publication and distribution of this paper as part of the ICAS proceedings or as individual off-prints from the proceedings.

References

[1] Richard Brown. Understanding the downwash/outwash characteristics of eVTOL aircraft. *Civil Aviation Authority*, 2023.

[2] Richard E Brown. Are eVTOL Aircraft Inherently More Susceptible To The Vortex Ring State Than Conventional Helicopters?

[3] Philip Tanner, Austin Overmeyer, Luther Jenkins, Chung-Sheng Yao, and Scott Bartram. Experimental Investigation of Rotorcraft Outwash in Ground Effect. In *Proceedings of the Vertical Flight Society 71st Annual Forum*, pages 1–26, Virginia Beach, VA, May 2015. The Vertical Flight Society.

[4] Andre Bauknecht, Clemens Schwarz, Markus Raffel, and Stephan Mailänder. Flow Measurement Techniques for Rotor Wake Characterization on Free-Flying Helicopters in Ground Effect. In *AIAA Scitech 2019 Forum*, San Diego, California, January 2019. American Institute of Aeronautics and Astronautics.

[5] Hasse N. J. Dekker, Daniele Ragni, Woutijn J. Baars, Fulvio Scarano, and Marthijn Tuinstra. Aerodynamic Interactions of Side-by-Side Rotors in Ground Proximity. *AIAA Journal*, 60(7):4267–4277, July 2022.

[6] Hasse N.J. Dekker, Woutijn J. Baars, Fulvio Scarano, Marthijn Tuinstra, and Daniele Ragni. Unsteady flow behaviour of multi-rotors in ground proximity. *Flow*, 3:E30, 2023.

[7] Seungcheol Lee, Seokbong Chae, Yisu Shin, and Jooha Kim. Aerodynamic effects of rotor–rotor interaction on a twin-rotor system in ground effect. *Journal of Fluid Mechanics*, 1031:A42, March 2026.

[8] B. Wieneke. Volume self-calibration for 3D particle image velocimetry. *Experiments in Fluids*, 45(4):549–556, October 2008.

[9] Daniel Schanz, Sebastian Gesemann, and Andreas Schröder. Shake-The-Box: Lagrangian particle tracking at high particle image densities. *Experiments in Fluids*, 57(5):70, May 2016.

[10] Young Jin Jeon, Markus Müller, Dirk Michaelis, and Bernhard Wieneke. Efficient reconstruction of flow field with pressure from particle tracks: Vic. *Bulletin of the American physical society*, 63, 2018.

[11] Jan F. G. Schneiders and Fulvio Scarano. Dense velocity reconstruction from tomographic PTV with material derivatives. *Experiments in Fluids*, 57(9):139, September 2016.